Journal of
Synchrotron Radiation

ISSN 0909-0495

Received 15 April 2009
Accepted 11 September 2009

Synchrotron study of oxygen depletion in a Bi-2212 whisker annealed at 363 K

Stefano Cagliero,[a]* Andrea Piovano,[b] Carlo Lamberti,[b]* Mohammad Mizanur Rahman Khan,[a] Angelo Agostino,[a] Giovanni Agostini,[b] Diego Gianolio,[b] Lorenzo Mino,[b] Juan A. Sans,[c] Chiara Manfredotti[d] and Marco Truccato[d]

[a]Department of General Chemistry and Organic Chemistry, NIS Centre of Excellence, University of Turin, Corso Massimo D'Azeglio 48, I-10125 Turin, Italy, [b]Department of Inorganic, Materials and Physical Chemistry, NIS Centre of Excellence and INSTM Unit, University of Turin, Via P. Giuria 7, I-10125 Turin, Italy, [c]European Synchrotron Radiation Facility (ESRF), 6 rue Jules Horowitz, BP 220, F-38043 Grenoble Cedex, France, and [d]Department of Experimental Physics, NIS Centre of Excellence, University of Turin, Via Giuria 1, I-10125 Turin, Italy. E-mail: stefano.cagliero@unito.it, carlo.lamberti@unito.it

Direct evidence is reported of structural and electronic effects induced on a single $Bi_2Sr_2CaCu_2O_{8+\delta}$ (Bi-2212) whisker during a progressive annealing process. The crystal was investigated by micro X-ray diffraction (μ-XRD), micro X-ray fluorescence and electrical characterization at the European Synchrotron Radiation Facility, during a series of three *in situ* thermal processes at 363 K. Each step increased the sample resistivity and decreased its critical temperature, up to a semiconducting behaviour. These data correlate with μ-XRD analysis, which shows an increase of the *c*-axis parameter from 30.56 Å to 30.75 Å, indicating an oxygen depletion mechanism. Mild temperature annealing could be an effective process to modulate the intrinsic Josephson junctions' characteristics in Bi-2212 whiskers.

Keywords: superconductor; microfocused X-ray beam; Bi-2212; whisker; THz; oxygen doping; Kirkpatrick–Baez mirrors; micro-XRF; micro-XRD.

1. Introduction

Electromagnetic emissions in the THz range have extensive applications for information and communication technologies, biology and medical sciences, non-destructive evaluation, global environmental monitoring and ultrafast computing (Tonouchi, 2007, and references therein). Materials for THz radiation solid-state sources are presently the subject of intensive research efforts. Several studies have been published describing the possibility of producing or sensing coherent THz radiation from layered high-temperature superconductors owing to their intrinsic Josephson junctions (IJJs) properties (Wang *et al.*, 2002; Ozyuzer *et al.*, 2007; Kadowaki *et al.*, 2008). Among the possible crystalline forms, Bi-2212 whiskers, owing to their microscopic size, are promising candidates for the fabrication of miniaturized devices (Kim *et al.*, 2003; Inomata, Kawae, Kim *et al.*, 2003; Badica *et al.*, 2006). Furthermore, some authors have reported on the possibility of controlling whisker IJJ parameters, *i.e.* the critical current density (J_c) and the junction resistance (R_N), by modifying the oxygen content, which is well known to be strongly related to the carrier density (Inomata, Kawae, Nakajima *et al.*, 2003; Kawae *et al.*, 2005). In previous publications we noticed that electrical characteristics modification of Bi-2212 whiskers, owing to oxygen content variation, was accompanied by structural modifications, indirectly measured by atomic force microscopy (AFM) (Truccato *et al.*, 2005; Cagliero *et al.*, 2007, 2009). In a previous paper, where we performed a structural study, only a single severely underdoped sample was measured, so that a correlation between measured *c*-axis and electrical properties was not possible (Truccato *et al.*, 2005).

Most of the diffraction studies present in the literature refer to data acquired on clusters of whiskers (Rahman Khan *et al.*, 2009; Cagliero *et al.*, 2009). This approach increases the intensity of the diffraction peaks but has severe drawbacks owing to averaging. Moreover, many measurements are reported in the literature showing double superconductive transitions in a single whisker, usually explained by the presence of intergrowths of different phases in the Bi–Sr–Ca–Cu–O system, which are not visible by structural analysis because of the low relative volumes (Inomata, Kawae, Nakajima *et al.*, 2003; Hatano *et al.*, 2001; Matsubara *et al.*, 1989). Moreover, such types of whiskers have been found to undergo modifications of the relative amount of the two constituent phases even at low temperatures (Truccato, Cagliero *et al.*, 2006). In order to avoid misinterpretation of the experimental results, in the present work we chose a single Bi-2212 whisker, previously electrically characterized, in order

to confirm the presence of a unique superconducting transition.

The problem of using a microscopic single whisker giving low intensity diffraction and fluorescence signals was overcome by the use of the ID22 synchrotron radiation microfocused beamline at ESRF, whose characteristics will be described in the experimental section. By means of this facility and also of microscopy techniques, the chemical composition, morphology and crystalline quality of the sample were first checked by micro X-ray fluorescence (μ-XRF), micro X-ray diffraction (μ-XRD), AFM and scanning electron microscopy (SEM) techniques. The crystal was then subjected to a three-step annealing process at 363 K aimed at progressively reducing the oxygen content. The process was monitored by following the evolution of both the *c*-axis parameter (μ-XRD) and the electrical properties (*R versus T*) of the Bi-2212 whisker. This multi-technical investigation allowed us to directly correlate structural properties and electrical behaviour of a single monophasic whisker during the superconducting to semiconducting transformation induced by thermal annealing.

2. Experiments

A Bi-2212 crystal was selected from a large batch obtained by the glassy precursor method (Truccato *et al.*, 2002). A chip for electrical measurement was obtained by mounting the whisker on a sapphire substrate where four point contacts were created by Ag physical vapour deposition. Such contacts were then covered with Au to avoid oxidation. With this sample the electrical and structural characterizations could be carried out on the same specimen during the three-step annealing process. The SEM micrograph (Fig. 1*a*) shows the whisker (indicated by the red arrow) and the four contacts perpendicular to the crystal (indicated by the four black arrows); the *a* and *b* crystallographic directions are also shown in the figure, with the *c*-axis pointing out of the plane of the paper. With this geometry the sample was electrically characterized along its *ab* crystallographic plane by the standard four-probe method with a 1 μA current. During the electrical measurements the sample was kept in He gas and the resistivity was recorded in the 77.6–295 K range. Possible effects on the sample electrical behaviour owing to the permanence in such an atmosphere or to differential thermal expansion between the whisker and the substrate are negligible, as discussed in previous papers by our group (Truccato, Cagliero *et al.*, 2006; Truccato, Agostino *et al.*, 2006).

The same chip was then mounted at the ID22 (Tucoulou *et al.*, 2008) beamline (label 5 in Fig. 1*b*). The angle between the sample holder and the beam (indicated by α in Fig. 1*b*) was adjusted during the XRD acquisition to catch (00*l*) Bragg reflections. The beam wavelength [λ = 0.72940 (7) Å], the sample-to-detector distance [110.596 (8) mm] and the detector tilt corrections have been determined from Rietveld refinement of an alumina standard. During the three-step annealing experiment the chip was alternately mounted and dismounted from the ID22 hutch to allow complementary μ-XRF–XRD and electrical characterization to be made on the same crystal. Micro-XRF maps were produced using the *PyMCA* code (Sole *et al.*, 2007) and μ-XRD data were analyzed by the *Fit2D* program developed by Hammersley at ESRF (Hammersley, 2004).

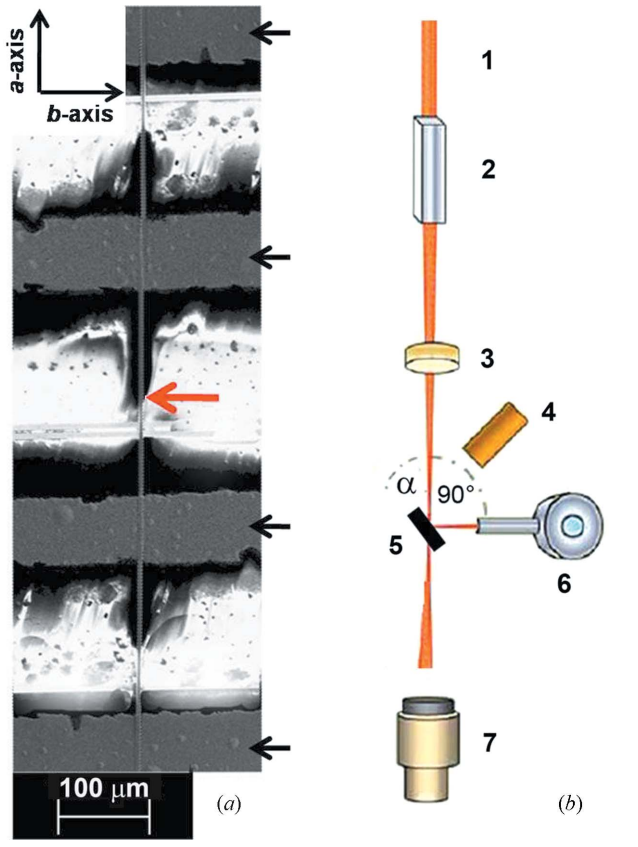

Figure 1
(*a*) SEM micrograph of the chip allowing both electrical and structural measurements. The Bi-2212 whisker lies vertically, along the whole figure height, and is indicated by the large red arrow. The four Ag/Au contacts run horizontally and are indicated by the four black arrows. The *a*- and *b*-axes are shown, with the *c*-axis pointing out of the plane of the paper. (*b*) Scheme of the experimental set-up adopted at the microfocused ID22 beamline for both μ-XRD and μ-XRF acquisitions. Details are labelled as follows: 1, incoming beam; 2, KB mirrors; 3, ionization chamber; 4, alignment microscope; 5, rotating sample holder allowing full α angle rotation; 6, XRF detector; 7, FreLoN detector for diffracted beam.

Regarding the beamline, ID22 is installed on a high-β straight section equipped with two different (U42 and U23) undulators (Tucoulou *et al.*, 2008). In the optic hutch a Pd-coated mirror, working at an incidence angle of 0.14°, has been used for harmonic rejection and a double-crystal Si(111) monochromator for λ selection. In the experimental hutch, the microprobe set-up consisted of Kirkpatrick–Baez (KB) mirrors (Riekel, 2000) (located 41 m from the source; label 2 in Fig. 1*b*). Using knife-edge scans, a spatial resolution of 1.7 μm (vertical) × 5.3 μm (horizontal) has been determined. With the efficiency of the KB mirrors reaching ∼70% and using both undulators together, the photon flux measured in the focal spot is about 10^9 photon s^{-1} at 17 keV for a ring current of 200 mA. The depth of focus is of the order of

300 µm. The incoming flux on the sample was continuously monitored by a mini-ionization chamber (label 3 in Fig. 1*b*), and a video-microscope (label 4) simplified the alignment of the sample and the microprobe set-up. The Si(Li) detector for µ-XRF (label 6) was placed at 90° with respect to the beam, while the FreLoN CCD detector (Suhonen *et al.*, 2007; Labiche *et al.*, 2007) was mounted behind the sample to allow µ-XRD measurements in transmission mode (label 7).

3. Results and discussion

As introduced above, the morphological, chemical and crystalline characteristics of the whisker were previously obtained for the as-grown whisker, which was then annealed following a three-step process and its evolution monitored from the electrical and structural points of view. In the following, both the preliminary measurements and the subsequent ones are described in chronological order, according to the annealing steps.

The electrical measurement of the as-grown sample found a single superconductive transition at T_c = 79.9 K, close to values previously observed in slightly overdoped whiskers grown by our group (Cagliero *et al.*, 2007). The corresponding resistivity data (ρ_{ab}) are plotted as a solid curve in Fig. 2. After the electrical measurement, the chip was mounted in the beamline as described above and the chemical homogeneity of the as-grown crystal was checked by µ-XRF maps (see Fig. 3). Figs. 3(*a*), 3(*b*) and 3(*c*) show Cu($K\alpha$)/Bi($L\alpha$), Sr($K\alpha$)/Bi($L\alpha$) and Cu($K\alpha$)/Sr($K\alpha$) maps, respectively, normalized to the incident beam intensity. Variations of about 4% noticeable along the crystal length (which is aligned along its *a*-axis) are of the same order of magnitude as the background noise. Consequently, the crystal, at this stage, was considered to have a uniform elemental distribution. The significant variation in the ratios observed in the bottom part of each map ($Y < 35$ µm) is due to the higher efficiency of Ag contacts (whose distribution is shown in Fig. 3*d*) in re-absorbing the lower-energy fluorescence lines, following the energy scale Cu($K\alpha$) < Bi($L\alpha$) < Sr($K\alpha$). In fact, Ag contacts, covering the whisker in the $Y < 35$ µm region, act as a high-energy filter for the fluorescence emitted by the whisker itself. Ca maps are not reported because of the very low signal-to-noise ratio.

The sample was then aligned for the µ-XRD measurement and single-crystal (00*l*) diffraction peaks were observed, as shown in Fig. 4(*a*). Powder rings owing to the Ag/Au contacts were also visible, which served as internal standards for adjusting both the sample-to-detector distance and the tilt angle parameters that underwent small variations along the three-step annealing process (mounting and dismounting the chip). Two main (00*l*) reflection series, owing to two crystalline domains misaligned by 14°, are visible and indexed as shown in the figure. Such crystalline domains are probably coupled by a small-angle grain boundary positioned along the *ac* plane, which in principle can arise from a series of edge dislocations stacked along the *c*-axis, similar to those observed in previous crystallographic studies on Bi-2212

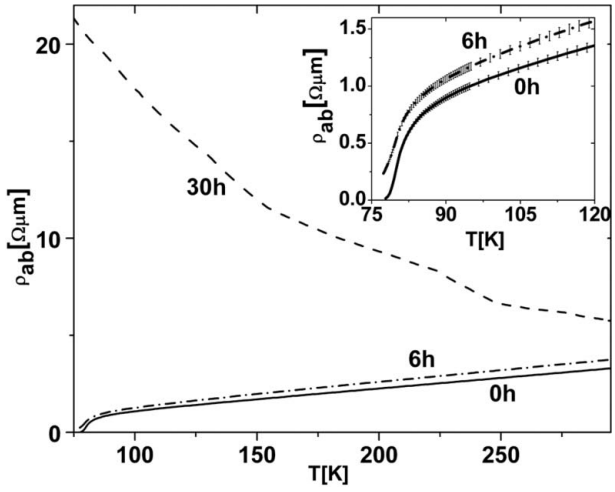

Figure 2
Summary of the three resistivity *versus T* measurements obtained on the Bi-2212 whisker during the three-step annealing process: solid curve, as-grown; dot-dashed curve, after 6 h at 363 K; dashed curve, after 30 h total annealing time at 363 K. The inset shows a zoom on the transition temperature for the measurements relative to the as-grown and 6 h-annealed sample. For each step the corresponding T_c, the resistivity value at 275 K and the *c*-axis parameter are reported in Table 1.

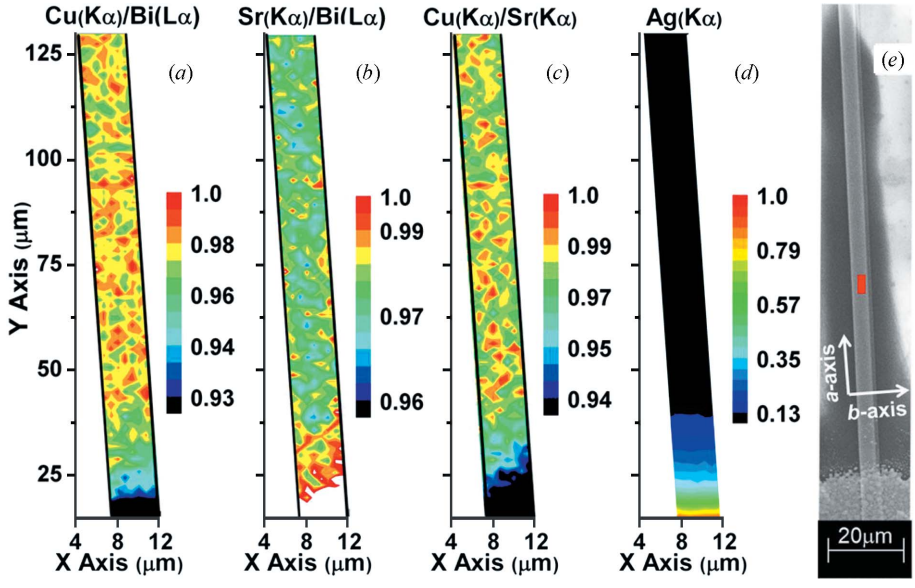

Figure 3
Maps of the X-rays fluorescence count ratios. Panels (*a*), (*b*) and (*c*) show Cu($K\alpha$)/Bi($L\alpha$), Sr($K\alpha$)/Bi($L\alpha$) and Cu($K\alpha$)/Sr($K\alpha$) normalized XRF count ratios, respectively. Panel (*d*) clarifies the Ag distribution. Panel (*e*) shows the SEM image of the same sample region: the red rectangle defines the beam dimension. The *a*- and *b*-axes are also shown, with the *c*-axis pointing out of the plane of the paper.

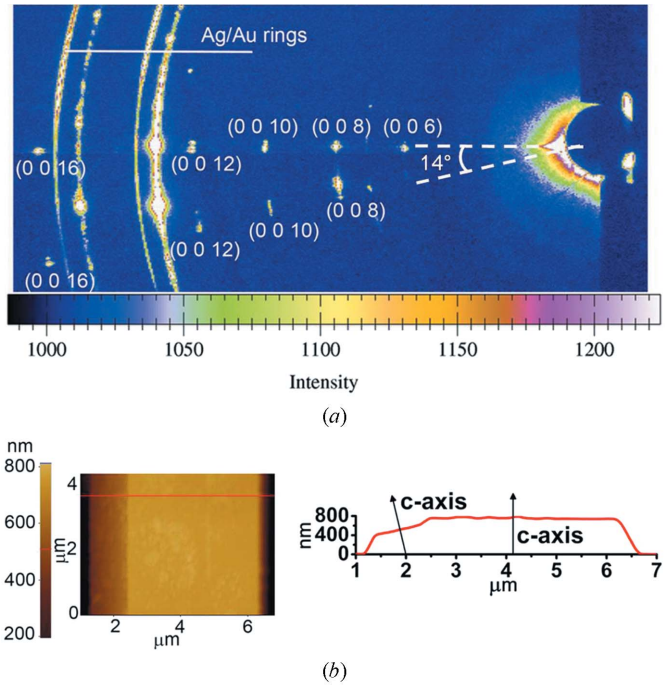

Figure 4
(*a*) μ-XRD image of the as-grown Bi-2212 crystal mounted on the chip. Two main series of (00*l*) reflections are visible with an angle of ∼14° between them. Diffraction rings from the Ag/Au contacts are also visible. (*b*) Two-dimensional AFM scanning of the sample showing that the upper surface profile is composed of two main planes misaligned by ∼14° (left). Thickness profile sampled along the red line (right).

whiskers (Timofeev & Gorlova, 1998; Krapf *et al.*, 1991). Moreover, Fig. 4(*b*) reports the whisker profile obtained by AFM, from which it can be noted that the upper surface of the crystal is formed by two main planes, misaligned by ∼14°. This angle is very similar to that observed by μ-XRD, thus it cannot be excluded that the whisker profile evidenced by AFM is due to the small-angle grain boundary discussed above. On the basis of these observations, we decided to evaluate the *c*-axis value by averaging the parameters obtained from the two series, which are in any case compatible within the error bars. This procedure was adopted during the whole experiment, a choice that is further justified by comparison between XRD and electrical measurements, as the latter involved the whole crystal volume between the voltage contacts (see Fig. 1*a*). Adopting this procedure, the *c*-axis of the as-grown sample was found to be 30.56 Å.

After these measurements the sample was heated in air at 363 K for 6 h and the resistivity and μ-XRD measurements were repeated, obtaining the dash-dotted curve in Fig. 2. The inset of the same figure underlines the increase of the resistivity (which is clearly outside the error bars) and the decrease of T_c, which reaches a value of 79.7 K. At this stage of annealing the *c*-axis parameter of the whisker was found to be 30.68 Å.

Finally, the sample underwent a further heating in air at 363 K, reaching a total heating time of 30 h. At this stage the electrical characterization showed a semiconducting behaviour for the whisker (Fig. 2), and the *c*-axis value of the crystal after this third step was evaluated to be 30.75 Å.

Table 1
Summary of the electrical and structural characteristics of the Bi-2212 whisker for the three annealing steps.

The total annealing hours, the critical temperature, the resistivity value at 275 K and the *c*-axis are given for each step of the process.

Annealing time (h)	T_c (K)	ρ_{ab} at 275 K (Ω μm)	*c*-axis (Å)
0	79.9	3.08	30.56
6	79.7	3.50	30.68
30	–	6.19	30.75

Micro-XRF maps, repeated after each annealing step, did not exhibit any significant difference with respect to those shown in Fig. 3 and are consequently not reported.

The evolution of all the relevant structural (*c*-axis parameters) and electrical (T_c and ρ_{ab} measured at T = 275 K) information along the three annealing steps are summarized in Table 1. The as-grown sample was found to be in the overdoped range according to the *c*-axis data reported by Inomata, Kawae, Nakajima *et al.* (2003). The decrease of the critical temperature, accompanied by the increase of its resistivity owing to the 6 h annealing, can be explained by an oxygen depletion process taking place in the crystal, as hypothesized in previous works by our group (Truccato, Cagliero *et al.*, 2006; Cagliero *et al.*, 2007), which is now clearly confirmed by the increase of the *c*-axis parameter. As a matter of fact, the new value of 30.68 Å belongs to the underdoped regime according to the scheme of reference (Inomata, Kawae, Nakajima *et al.*, 2003). The oxygen depletion was found to greatly increase the whisker resistivity after the second annealing step, which brought the total annealing time to 30 h. At this stage a further *c*-axis increase shifts the sample deeply into the underdoped regime (Inomata, Kawae, Nakajima *et al.*, 2003), as confirmed by the dramatic changes in the electrical properties, *i.e.* the absence of the metal resistivity behaviour and disappearance of the superconducting transition (Fig. 2). Referring to the work by Inomata *et al.*, we should emphasize that data reported therein were obtained on whiskers synthesized from tellurium-doped precursors, thus T_c and *c*-axis values could be slightly shifted with respect to our work (which used an undoped precursor method). Finally, for the sake of completeness, we should also take into account that beam heating may play a role in the overall-annealing process. Using the X-ray beam characteristics and the whisker thickness crossed by the beam (0.4–1 μm), we estimated a maximum absorbed power density of about 3×10^5 W m^{-2}. The local temperature increase on the sample owing to photon heating could not be evaluated owing to the very complex sample and environmental geometry (whisker, air, silver contacts and sapphire substrate), making it very hard to foresee all the heat transfer processes, which goes beyond the scope of this work. Dedicated future experiments should be useful to discriminate between the furnace annealing and the radiation heating effects.

4. Concluding remarks

We have reported direct evidence of the oxygen depletion process in a single Bi-2212 whisker, by combining *in situ* resistivity *versus* temperature and μ-XRD measurements. We have correlated the *c*-axis elongation observed during a three-step annealing process at 363 K, with electrical property modifications, ranging from an overdoped regime to a complete underdoped semiconductive behaviour. The whole data set was obtained *in situ* on a unique monophasic whisker. This study extends data reported in previous publications, envisaging possible tuning of the IJJs' properties in THz devices of micrometric size, and in the understanding of the aging process occurring in Bi-2212 whiskers.

The experiment at ESRF ID22 was performed in the frame of proposal CH-2654. G. Cotto (University of Turin), Carmelo Prestipino (ESRF during experiment CH-2654, presently at University of Rennes-1) and G. Martinez-Criado (ESRF) significantly contributed to the success of this experiment.

References

Badica, P., Togano, K., Awaji, S., Watanabe, K. & Kumakura, H. (2006). *Supercond. Sci. Technol.* **19**, R81–R99.

Cagliero, S., Agostino, A., Bonometti, E. & Truccato, M. (2007). *Supercond. Sci. Technol.* **20**, 667–671.

Cagliero, S., Agostino, A., Khan, M. M. R., Truccato, M., Orsini, F., Marinone, M., Poletti, G. & Lascialfari, A. (2009). *Appl. Phys. A*, **95**, 479–484.

Hammersley, A. (2004). *FIT2D*, http://www.esrf.eu/computing/scientific/FIT2D/FIT2D_REF/fit2d_r.html.

Hatano, T., Takano, Y., Ishii, A., Fukuyo, A., Arisawa, S. & Togano, K. (2001). *Physica C*, **362**, 296–300.

Inomata, K., Kawae, T., Kim, S., Nakajima, K., Yamashita, T., Sato, S., Nakajima, K. & Hatano, T. (2003). *Supercond. Sci. Technol.* **16**, 1365–1367.

Inomata, K., Kawae, T., Nakajima, K., Kim, S. J. & Yamashita, T. (2003). *Appl. Phys. Lett.* **82**, 769–771.

Kadowaki, K., Yamaguchi, H., Kawamata, K., Yamamoto, T., Minami, H., Kakeya, I., Welp, U., Ozyuzer, L., Koshelev, A., Kurter, C., Gray, K. E. & Kwok, W. K. (2008). *Physica C*, **468**, 634–639.

Kawae, T., Nagao, M., Takano, Y., Wang, H., Hatano, T. & Yamashita, T. (2005). *Physica C*, **426**, 1479–1483.

Kim, S. J., Hatano, T., Kim, G. S., Kim, H. Y., Nagao, M., Inomata, K., Yun, K. S., Takano, Y., Arisawa, S., Ishii, A., Takahashi, S., Chen, J., Nakajima, K. & Yamashita, T. (2003). *Physica C*, **412**, 1401–1405.

Krapf, A., Lacayo, G., Kastner, G., Kraak, W., Pruss, N., Thiele, H., Dwelk, H. & Hermann, R. (1991). *Supercond. Sci. Technol.* **4**, 237–238.

Labiche, J. C., Mathon, O., Pascarelli, S., Newton, M. A., Ferre, G. G., Curfs, C., Vaughan, G., Homs, A. & Carreiras, D. F. (1991). *Rev. Sci. Instrum.* **78**, 091301.

Matsubara, I., Tanigawa, H., Ogura, T., Yamashita, H., Kinishita, N. & Kawai, T. (1989). *Jpn. J. Appl. Phys.* **28**, L1358–L1360.

Ozyuzer, L., Koshelev, A. E., Kurter, C., Gopalsami, N., Li, Q., Tachiki, M., Kadowaki, K., Yamamoto, T., Minami, H., Yamaguchi, H., Tachiki, T., Gray, K. E., Kwok, W. K. & Welp, U. (2007). *Science*, **318**, 1291–1293.

Rahman Khan, M. M., Cagliero, S., Agostino, A., Beagum, M., Plapcianu, C. & Truccato, M. (2009). *Supercond. Sci. Technol.* **22**, 085011.

Riekel, C. (2000). *Rep. Prog. Phys.* **63**, 233–262.

Sole, V. A., Papillon, E., Cotte, M., Walter, Ph. & Susini, J. (2007). *Spectrochim. Acta B*, **62**, 63–68.

Suhonen, H., Fernández, M., Bravin, A., Keyriläinen, J. & Suortti, P. (2007). *J. Synchrotron Rad.* **14**, 512–521.

Timofeev, V. N. & Gorlova, I. G. (1998). *Physica C*, **309**, 113–119.

Tonouchi, M. (2007). *Nat. Photon.* **1**, 97–105.

Truccato, M., Agostino, A., Rinaudo, G., Cagliero, S. & Panetta, M. (2006). *J. Phys. Condens. Matter*, **18**, 8295–8318.

Truccato, M., Cagliero, S., Agostino, A., Panetta, M. & Rinaudo, G. (2006). *Supercond. Sci. Technol.* **19**, 1003–1009.

Truccato, M., Lamberti, C., Prestipino, C. & Agostino, A. (2005). *Appl. Phys. Lett.* **86**, 213116.

Truccato, M., Rinaudo, G., Manfredotti, C., Agostino, A., Benzi, P., Volpe, P., Paolini, C. & Olivero, P. (2002). *Supercond. Sci. Technol.* **15**, 1304–1310.

Tucoulou, R., Martinez-Criado, G., Bleuet, P., Kieffer, I., Cloetens, P., Labouré, S., Martin, T., Guilloud, C. & Susini, J. (2008). *J. Synchrotron Rad.* **15**, 392–398.

Wang, H. B., Wu, P. H., Chen, J., Maeda, K. & Yamashita, T. (2002). *Appl. Phys. Lett.* **80**, 1604–1606.